FINAL TECHNICAL REPORT

AWARD NUMBERS: G18AP00049 (AECOM) and G18AP00050

(UAF)

A suite of kinematic rupture models for the 1964 Alaska earthquake, Collaborative Research with AECOM Technical Services and the University of Alaska, Fairbanks

Principal Investigators:

Dr Hong Kie Thio

AECOM Technical Services
300 S Grand Ave
Los Angeles, CA 90071
hong.kie.thio@aecom.com
323-996-2225

Dr. Carl Tape

University of Alaska, Fairbanks
903 Koyukuk Drive
Fairbanks, AK 99775-7320
ctape@alaska.edu
907-474-5456

Start and End dates:

2018/07/01 – 2020/06/30

ABSTRACT

This report presents the results of a multi-faceted study of ground motion simulations for realistic slip scenarios of the 1964 Alaska earthquake. The slip scenarios are obtained through a combination of inversion of observed data (seismic, geodetic and tsunami) and suite of forward models to bracket the potential dynamic parameters such as rise-time. Slip models that are consistent with the data are then used as input to 3-D simulations of ground motions in the Cook Inlet region (including Anchorage) using a realistic basin model of the area, as well as the best available 3D tomographic model for the crust and uppermost mantle. The computed timeseries are finally augmented with stochastically derived high-frequency signals using a matched filter to produce broad-band 3D ground motions

1 Introduction

The 1964 Alaska earthquake is the largest subduction zone earthquake in recorded history and is still of great interest in our understanding of earthquake process and the ground motions associated. While the earthquake occurred after the deployment of the Word-wide Standardized Seismographic Network (WWSSN), observations are still scarce, and limited to the P waves of recorded at long-period WWSSN and Galitzin stations, marigrams from several stations in California, Hawaii and Alaska and local levelling and triangulation data.

While the earthquake slip has been analyzed before, it remains poorly constrained due to the aforementioned limitations in data.

In order to gain a better understanding of the ground motions due to the 1964 earthquake, and future events in the area, we re-analyzed the rupture process of the earthquake with a focus on the range of acceptable (from an observational point of view) solutions and the ground motions that they generate.

This project therefore consists of two main tasks:

- Finding a range of acceptable slip models
- Computing local ground motions using a 3-D model of the Anchorage region

2 Source geometry

For the source geometry we used the Slab2.0 model (Hayes et al., 2018). The subduction zone interface is initially sampled with 2 x 1 km fault patches that follow the curvature of the interface. This set of patches is then resampled to approximately 40x20 km subfaults that are used for the actual inversion. The static Green's functions however, are computed for these subfaults using the original patches that comprise every subfault, therefore keeping the curved rupture even at the coarser level (Figure 1). This model is both more accurate, in terms of geometry, and also higher resolution than the Ichinose et al. (2007) study. In addition, we used a FK-integration technique to compute the static displacements at the surface with a 1D model (Wang et al., 2003, 2006). The improved geometry will give more reliable results for the inversion. The higher resolution grid may be necessary for the added triangulation data, but it is more importantly meant to improve the accuracy of the subsequent ground motion calculations. In fact, for the inversion, the greater number of subfaults means that we regularization of the inverse process becomes very important.

3 Source inversion

Seismic and geodetic data are inverted for fault slip using the multiple-time window algorithm of Thio et al. (2004), which is a modified form of Hartzell and Heaton (1983). A least squares inversion with mixed constraints is applied using Lawson and Hanson (1974). The rake angle of the slip can vary within +/- 45°of a target rake, which in this case corresponds to the average normal to the trench.

The inversion algorithm includes the option of a smoothing constraint, which, but no damping constraint on the slip and used nominally rectangular sub-faults of 20 by 10 km

covering a depth range from 0 km at the trench to 45 km deep along the subduction interface. The inversion can simultaneously solve for a baseline shift in the geodetic data.

A more detailed description of the inversion procedure can be found in Thio et al (2004). While the Ichinose et al. (2007) paper is the starting point for the current study, there are some substantial differences between the that paper and the current analysis (Table 1).

In the course of this project, it became clear that the initial plan of producing a few dozen different rupture models for the subsequent modeling became unpractical, due to the many degrees of freedom in the inversion procedure relative to the amount and quality of the data. In particular, the dynamic properties such as rise-time are very poorly constrained. We therefore have resorted to a combination of inverse solutions and within these results vary the dynamic rise-time systematically, re-compute the seismic and tsunami synthetics and analyze the fit to the data. This hybrid inverse-forward modeling procedure gives us more control of the process while still allowing us the search for semi-objective fits to the data.

Another issue arose for the use of the tsunami data. While originally we planned to use the method of Watada et al (2014) to correct the tsunami data for the solid Earth response to the tsunami waveforms, this proved to be impractical with the quality of the data so instead we ae using the JAGURS code (Baba et al., 2017), a modern development based on the original Satake (1995) code used by Ichinose et al(2007) to do the forward computations of the tsunami waves. While this has made the tsunami calculations more expensive computationally, it makes much better use of the recorded tsunami data then only using the linear tsunami waveforms in the inversion.

Table 1 Main differences between the Ichinose et al (2007) study and the current analysis.

	Ichinose et al., 2007	This study
Source parametrization		
Subfault size	50x50 km	~40x20 km
Number of subfaults	95	545
Extent	147W-154W	144W-157W
Plane	2 rectangular	curved
Data		
P-waves	35	35
Leveling	48	48
Triangulation	-	~200
Tsunami	9	11
Modeling		
Tsunami grid	2 arcmin-30 arcsec	15 arcsec
Static displacement	Okada, halfspace	FK integration, 1D

4 Inversion results

So far we have explored a range of inversion parameters that are needed to produce stable results based on the available data. We are looking at several features that are of importance either from a tectonic perspective or from a ground motion prediction perspective. An example of the former is the delineation of the rupture extent towards the west (into the 1938 rupture zone) and to the east, as well as the down-dip extent of the rupture. For the ground motions, the constraints on the main asperities are of great importance, with the rise-time explored further in a more forward sense.

In Figure 2 we present several slip distributions that are distinctly different yet provide a similar fit with the data (Figure 3). Currently, we have explored variations in smoothing and rupture velocities but in the future may also address different weighting schemes for the data. These models include the levelling data as well, but not yet the triangulation data which was a late addition to the project, and which needs some special treatment to account for baseline issues. While the large-scale slip distribution is quite stable in these results, there are significant differences in lateral rupture extent (in the case of increased rupture velocity) and roughness (for different smoothness parameters). We will explore these sensitivities further with addition of the triangulation data and, in the case of the rupture extent, the forward computation using the JAGURS code. The more accurate timings yielded by that code will allow us to analyze the tsunami arrivals with absolute time. Because the speed of tsunamis is much lower than the rupture speed of earthquakes, the first arriving tsunami wave emanates from the part of the rupture closest (in travel-time) to the tide-gauge station.

In Figure Figure 4 we compare the rupture characterization from the original Ichinose et al (2007) study and one of the current models as they are used for the 3-D simulations.

5 Ground motions

5.1 3D seismic wavefield simulations 3D velocity model

The Earth structure model is that of Nayak et al. (2020), with an embedded model of Cook Inlet basin (Shellenbaum et al., 2010). The Cook Inlet basin extends approximately 200 km in the slab-parallel direction and 100 km in the slab-normal direction and has a maximal depth of 7.6 km (Shellenbaum et al., 2010). It lies above the 40–80 km slab seismicity and is adjacent to the boundary of the aftershock zone of the Mw 9.2 Alaska earthquake. Due to its oil and gas deposits and proximity to Anchorage (population 374,000), Cook Inlet basin is the best studied basin in Alaska (e.g., Fisher and Magoon, 1978; Haeussler et al., 2000) and is the only basin with a publicly available digital map of its basement geometry (Shellenbaum et al., 2010). The effects of Cook Inlet basin (west of Anchorage) on the wavefield are quite apparent in the simulations (e.g., Figure 6) and in data from local earthquakes and ambient noise (Smith and Tape, 2019).

5.1.1 Mesh

We generate finite element meshes with hexahedral elements using the internal mesher in SPECFEM3D (Komatitsch et al., 2004; Peter et al., 2011). Our unstructured meshes are de-

signed to optimally handle slow wave speeds near the surface and faster wave speeds in the upper mantle.

The finite element mesh in Tape (2014) contained 4,696,704 hexahedral elements that are largest at the bottom of the mesh, at 400 km below sea level, and smallest at the topographic surface. There are 312 million gridpoints in the mesh; the gridpoint spacing at the surface is about 200 m. The topographic detail that is visible is the actual top surface of the mesh.

In our latest effort, the simulation region was broadened to accommodate the possibility of a larger rupture region for the 1964 earthquake (Figure 1). The volume we used was extended by 200 km to the west and 100 km to the south, giving an area of 1400 km x 700 km. The mesh contains three doubling layers and a total of 6,291,456 elements and 414,092,544 gridpoints. An example of one partition of a mesh is shown in Figure 7.

5.1.2   Simulations

Our seismic wavefield simulations were performed on 256 cores of the the chinoook cluster, which is part of UAF Geophysical Institute's Research Computing Systems. The simulations used a timestep of 0.012 s and iterated 43,000 time steps (516 s of seismogram time). The calculation took 2 hours and 34 minutes. The half duration for each subsource was fixed as 2 s. This parameter is uncertain from the source estimation, which cannot constrain the details of the rise time for each subsource. Nevertheless, the half duration needs to be sufficiently small in order to achieve a reasonable smooth rupture and for the wavefield to "see" the 3D structural heterogeneity in the crust, notably Cook Inlet basin.

The accuracy of the synthetic seismograms was verified by direct comparison with 1D synthetics from the toolkit of AxiSEM (Nissen-Meyer et al., 2014), Instaseis (van Driel et al., 2015), and Syngine (Krischer et al., 2017). The 1D and 3D synthetics are similar in their amplitudes and shape, suggesting that both codes are correctly implementing the input finite source model for the 1964 earthquake. The differences between the 1D and 3D synthetics are on the order of meters for both the dynamic and static displacements (Figure 8), with the largest differences occurring in the Cook Inlet region, west of Anchorage (Figure 9**Error! Reference source not found.**).

5.2   High frequencies

5.2.1   Method

The high-frequency portion of the simulations are performed using the stochastic finite-fault method EXSIM (Motazedian and Atkinson, 2005). EXSIM subdivides an earthquake rupture into a grid of subsources and applies the stochastic point source method to each of them (Figure 4**Error! Reference source not found.**). A stochastic point source waveform is then obtained for each subsource, and these are summed in the time domain to estimate the total synthetic at a site. Each subsource is activated with delay time based on rupture propagation from the hypocenter to the subsource.

Details of the stochastic method are not discussed here in detail, but the interested reader is referred to the relevant literature (e.g., Hanks and McGuire, 1981; Boore, 1983, 2009; Boore and Atkinson, 1987; Atkinson and Boore, 1997). In this study, stochastic finite-fault modeling is

implemented by incorporating modifications suggested by Boore (2009), Atkinson et al. (2009), and Ghofrani et al. (2017). These improvements include (i) scaling of high-frequency motions based on the integral of squared acceleration spectrum, rather than velocity spectrum; (ii) no truncation of subsource time-histories (Boore, 2005); and (iii) the performance in the low-frequency range is improved (Ghofrani et al., 2017).

Table 2 The EXSIM model parameters.

Model Parameters	Value/Model
Fault Dimensions	1,120 (max length along strike) x 630 (max width down dip) km
Subfault Dimension	40 x 25 km
Slip Distribution and Hypocenter	This study (Figure X)
Stress Parameter	300 bars
Shear Wave Velocity (Bs)	3.7 km/s
Density (ps)	2.8 g/cm3
Rupture Propagation Velocity	0.8Bs
Crustal Amplification Model	Boore and Joyner (1997)
Duration Model	Boore and Thompson (2014)
Geometrical Spreading	b^-1 for R<40 km, b^0.5 for R>40 km
Q-Model	Atkinson (1995); 263f^0.5 after Frankel et al (2018)
Kappa	0.025 s

5.2.2   Combining the Low- and High-Frequency Results

We use the Graves and Pitarka (2010, 2018) filtering and summation method to combine the low- and high-frequency simulations into a broadband result. This method uses a set of 4th order zero-phase Butterworth filters. A high-pass filter is applied to the HF simulation (EXSIM) and a low-pass filter is applied to the LF simulation; these filters sum to unity across all frequencies (Figure 10). We use a corner frequency at fmatch = 0.5 Hz. The filtering is done in the time domain and the broadband response is obtained by summing the filtered results (Figure 11).

5.2.3   Results at NE004 and SE008

Results for two representative stations are provided. Station NE004 is located approximately 100 km southwest of Anchorage and directly above the earthquake rupture, and to the west of the hypocenter and areas of highest slip. Station SE008 is located near the eastern extent of the rupture at the mouth of the Bering river.

6 Conclusion

This project has yielded promising results for the future computation of 3D ground motions for seismic hazard applications. In the very near future, several steps will be undertaken to improve on the current results, some of which have already alluded to in the main text.

For the inversion, the addition of the triangulation data will improve the constraints on the final rupture models, the forward computations of different rise times will yield a wider range of compatible models for ground motion modeling and the use of the JAGURS tsunami code will provide a more reliable check on the rupture extent due to improved accuracy in travel times. Many of the stochastic model parameters are taken from Frankel et al (2018) [Cascadia], Ghofrani et al., (2017) [Tohoku], and these relied on empirical calibrations from a wide range of geographies and styles of earthquakes. These should be calibrated for earthquakes the Alaska subduction zone.

7 Data availability

The data will be made openly available on-line at the following repository:

https://scholarworks.alaska.edu/handle/11122/11886

8 Acknowledgment of support and disclaimer

9 Bibliography

It is expected that this work will submitted to a peer-reviewed journal later this year, and we will notify the NEHRP Grant administration upon publication.
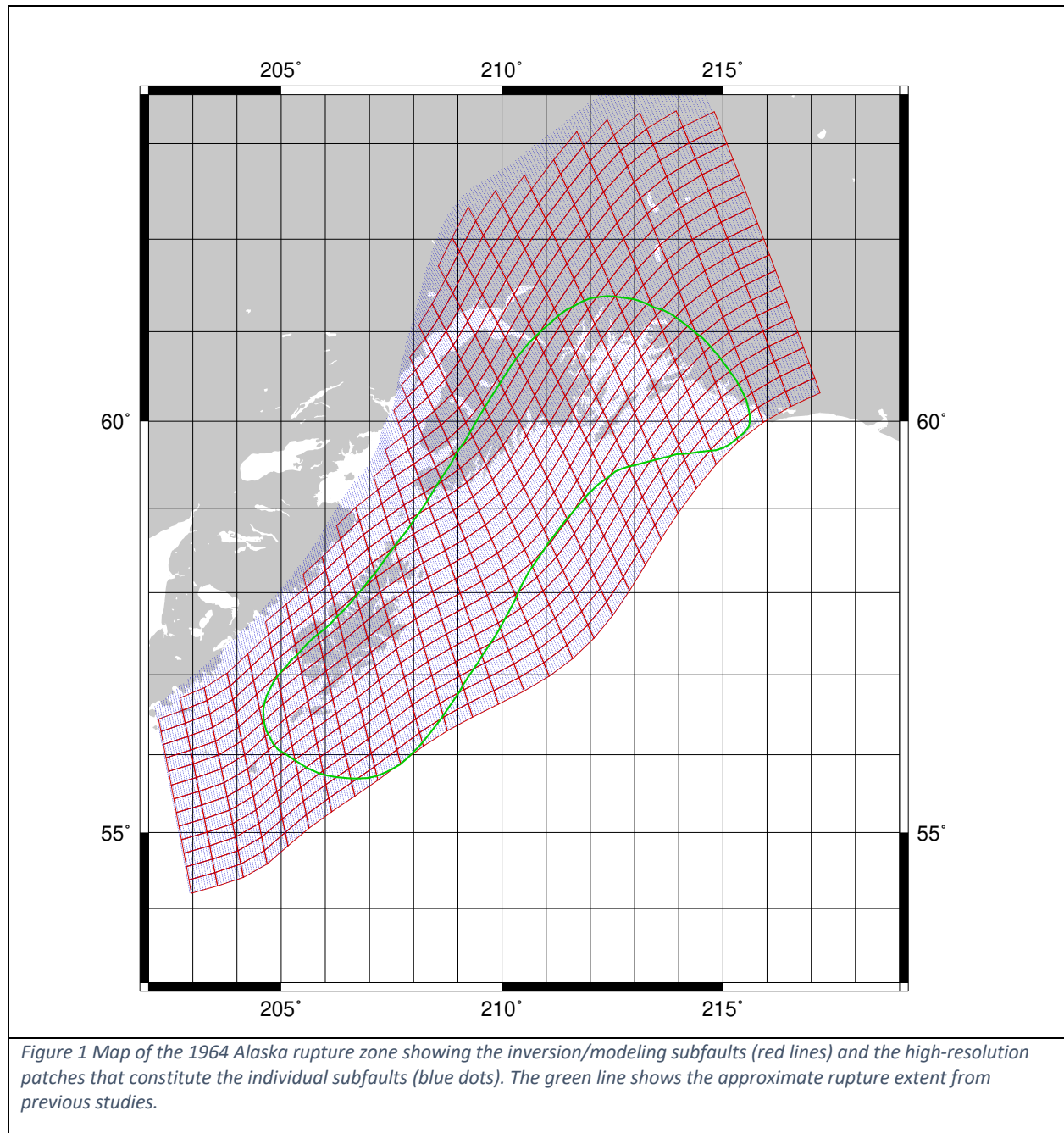
10 References

Baba T, Allgeyer S, Hossen J, Cummins PR, Tsushima H, Imai K, Yamashita K, Kato T (2017) Accurate numerical simulation of the far-field tsunami caused by the 2011 Tohoku earthquake, including the effects of Boussinesq dispersion, seawater density stratification, elastic loading, and gravitational potential change. Ocean Model 111:46–54.

Christensen, D. H., and S. L. Beck (1994), The rupture process and tectonic implications of the great 1964 Prince William Sound earthquake, Pure App. Geophys., 142(1), 29–53.

Christeson, G. L., S. P. S. Gulick, H. J. A. van Avendonk, L. L. Worthington, R. S. Reece, and T. L. Pavlis (2010), The Yakutat terrane: Dramatic change in crustal thickness across the Transition fault, Alaska, Geology, 38(10), 895–898.
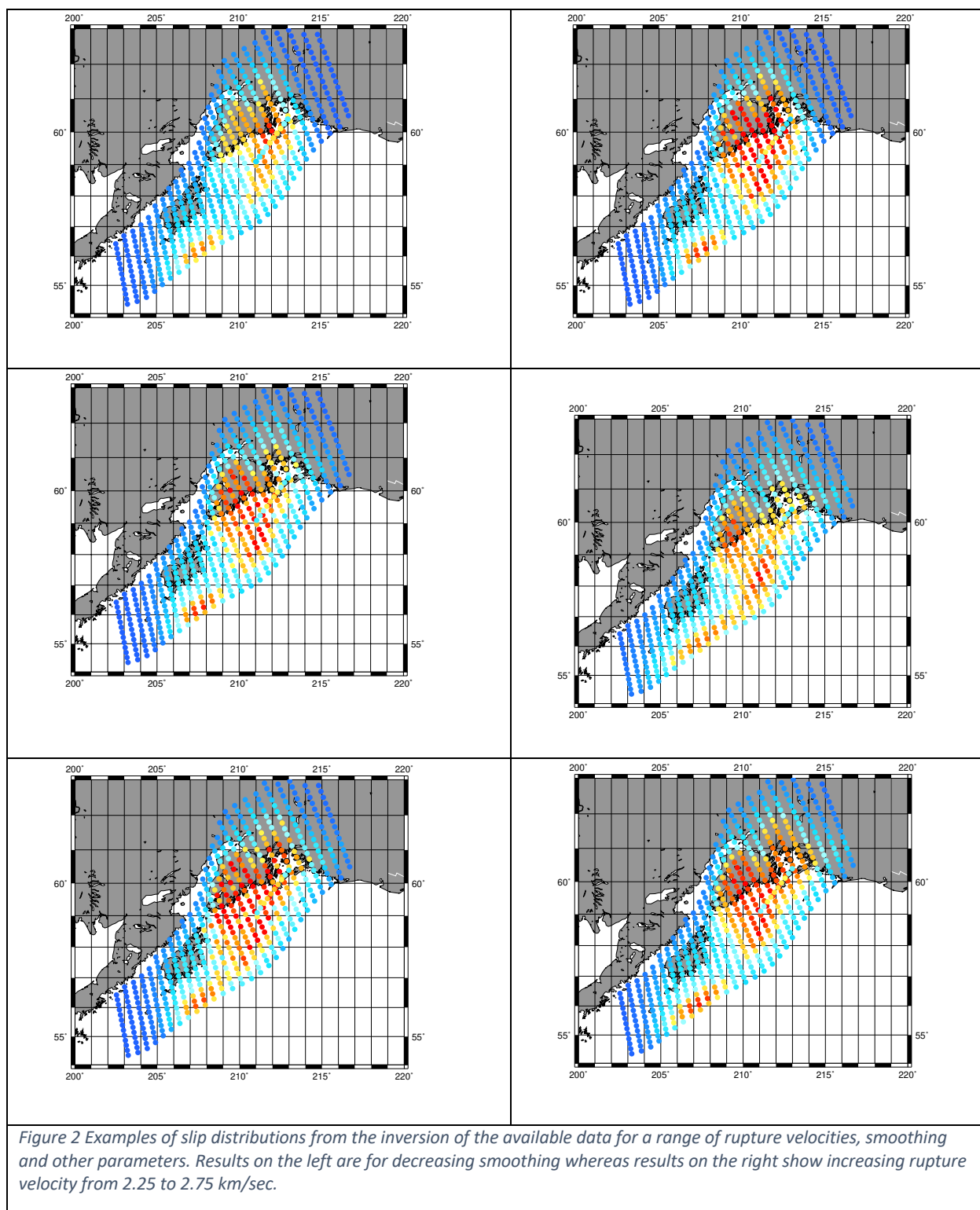
Eberhart-Phillips, D., P. J. Haeussler, J. T. Freymueller, A. D. Frankel, C. M. Rubin, P. Craw, N. A. Ratchkovski, G. Anderson, G. A. Carver, A. J. Crone, T. E. Dawson, H. Fletcher, R. Hansen, E. L. Harp, R. A. Harris, D. P. Hill, S. Hreinsd́ottir, R. W. Jibson, L. M. Jones, R. Kayen, D. K. Keefer, C. F. Larsen, S. C. Moran, S. F. Personius, G. Plafker, B. Sherrod, K. Sieh, N. Sitar, and W. K. Wallace (2003), The 2002 Denali fault earthquake, Alaska: A large magnitude, slip- partitioned event, Science, 300, 1113–1118.

Eberhart-Phillips, D., D. H. Christensen, T. M. Brocher, R. Hansen, N. A. Ruppert, P. J. Haeussler, and G. A. Abers (2006), Imaging the transition from Aleutian subduction to Yakutat collision in central Alaska, with local earthquakes and active source data, J. Geophys. Res., 111, B11303, doi:10.1029/2005JB004240.

Fisher, M. A., and L. B. Magoon (1978), Geologic framework of lower Cook Inlet, Am. Assoc. Petroleum Geol. Bull., 62(3), 373–402.

Graves, R., T. H. Jordan, S. Callaghan, E. Deelman, E. Field, G. Juve, C. Kesselman, P. Maechling, G. Mehta, K. Milner, D. Okaya, P. Small, and K. Vahi (2011), CyberShake: A physics-based seismic hazard model for southern California, Pure App. Geophys., 168, 367–381.

Haeussler, P. J., R. L. Bruhn, and T. L. Pratt (2000), Potential seismic hazards and tectonics of the upper Cook Inlet basin, Alaska, based on analysis of Pliocene and younger deformation, Geol. Soc. Am. Bull., 112(9), 1414–1429.

Hayes, G.P., Moore, G.L., Portner, D.E., Hearne, M., Flamme, H., Furtney, M. and Smoczyk, G.M., 2018. Slab2, a comprehensive subduction zone geometry model: *Science*, **362**, p. 58–61, doi: 10.1126/science.aat4723.

Holdahl, S. R., and J. Sauber (1994), Coseismic slip in the 1964 Prince William Sound earthquake: A new geodetic inversion, Pure App. Geophys., 142(1), 55–82, doi:10.1007/BF00875968.

Ichinose, G., P. Somerville, H. K. Thio, R. Graves, and D. O'Connell (2007), Rupture process of the 1964 Prince William Sound, Alaska, earthquake from the combined inversion of seismic, tsunami, and geodetic data, J. Geophys. Res., 112, B07306, doi:10.1029/2006JB004728.

Johnson, J. M., and K. Satake (1994), Rupture extent of the 1938 Alaskan earthquake as inferred from tsunami waveforms, Geophys. Res. Lett., 21(8), 733–736.

Johnson, J. M., K. Satake, S. R. Holdahl, and J. Sauber (1996), The 1964 Prince William Sound earthquake: Joint inversion of tsunami and geodetic data, J. Geophys. Res., 101(B1), 523–532.

Komatitsch, D., Q. Liu, J. Tromp, P. Su̇ss, C. Stidham, and J. H. Shaw (2004), Simulations of ground motion in the Los Angeles basin based upon the spectral-element method, Bull. Seis- mol. Soc. Am., 94(1), 187–206, doi:10.1785/0120030077.

Krischer, L., A. R. Hutko, M. van Driel, S. Sẗahler, M. Bahavar, C. Trabant, and T. Nissen- Meyer (2017), On-demand custom broadband synthetic seismograms, Seismol. Res. Lett., 88 (4), 1127–1140, doi:10.1785/0220160210.

Nayak, A., D. Eberhart-Phillips, N. Ruppert, H. Fang, M. M. Moore, C. Tape, D. H. Christensen, G. A. Abers, and C. Thurber (2020), 3D seismic velocity models for Alaska from joint tomographic inversion of body-wave and surface-wave data, Seismol. Res. Lett., 91 (6), 3106–3119, doi:10.1785/ 0220200214.
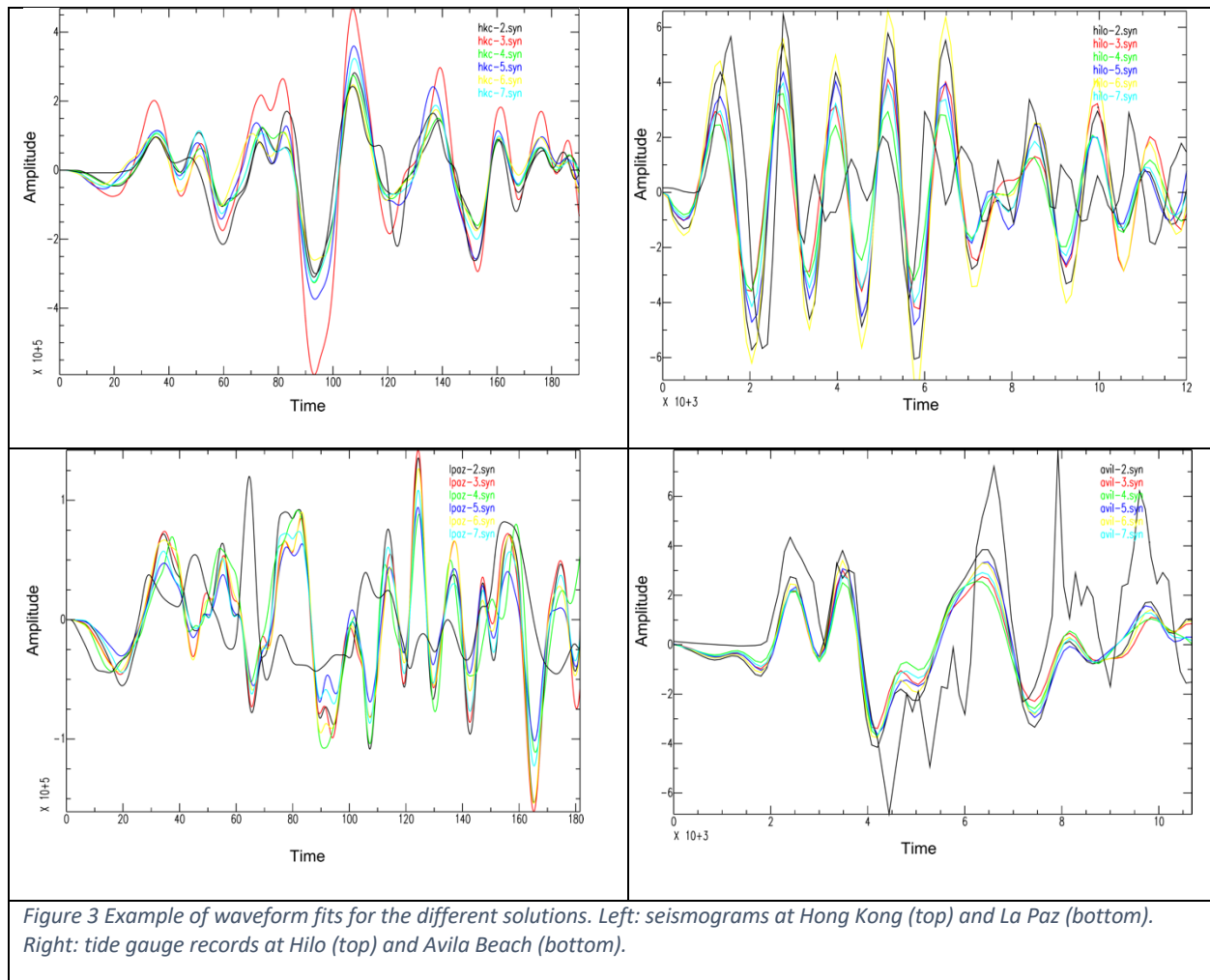
Nettles, M., and G. Ekstr̈om (2014), CMT re-analysis of the great 1964 Alaska earthquake, Abstract presented at the 2014 SSA Annual Meeting, Anchorage, Alaska, April 30 - May 2.

Nissen-Meyer, T., M. van Driel, S. C. Sẗahler, K. Hosseini, S. Hempel, L. Auer, A. Colombi, and A. Fournier (2014), AxiSEM: broadband 3-D seismic wavefields in axisymmetric media, Solid Earth, 5, 425–445, doi:10.5194/se-5-425-2014.

Peter, D., D. Komatitsch, Y. Luo, R. Martin, N. Le Goff, E. Casarotti, P. Le Loher, F. Magnoni, Q. Liu, C. Blitz, T. Nissen-Meyer, P. Basini, and J. Tromp (2011), Forward and adjoint simu- lations of seismic wave propagation on fully unstructured hexahedral meshes, Geophys. J. Int., 186, 721–739.

Rondenay, S., L. G. J. Mont́esi, and G. A. Abers (2010), New geophysical insight into the origin of the Denali volcanic gap, Geophys. J. Int., 182, 613–630.

Satake, K. (1995), Linear and nonlinear computations of the 1992 Nicaragua earthquake Tsunami, Pure Appl. Geophys., 144, 455–470.

Shellenbaum, D. P., L. S. Gregersen, and P. R. Delaney (2010), Top Mesozoic unconformity depth map of the Cook Inlet Basin, Alaska, doi:10.14509/21961, Alaska Div. Geol. Geophys. Surv. Report of Investigation 2010-2, 1 sheet, scale 1:500,000, available at http://www.dggs.alaska.gov/pubs/id/21961 (last accessed 2016-10-30).

Smith, K., and C. Tape (2019), Seismic response of Cook Inlet sedimentary basin, southern Alaska, Seismol. Res. Lett., 91(1), 33–55, doi:10.1785/0220190205.

Suito, H., and J. T. Freymueller (2009), A viscoelastic and afterslip postseismic deformation model for the 1964 Alaska earthquake, J. Geophys. Res., 114, B11404, doi:10.1029/2008JB005954.

Suleimani, E. (2011), Numerical Studies of Tectonic and Landslide-Generated Tsunamis caused by the 1964 Great Alaska Earthquake, Ph.D. thesis, University of Alaska Fairbanks, Fairbanks, Alaska, USA.

Suleimani, E. N., R. A. Hansen, and Z. Kowalik (2003), Inundation modeling of the 1964 tsunami in Kodiak Island, Alaska, in Sumbarine Landslides and Tsunamis, NATO Science Series IV: Earth and Environmental Sciences, vol. 21, edited by A. C. Yaļciner, E. N. Pelinovsky, E. Okal, and C. E. Synolakis, pp. 191–201, Kluwer Academic, Dordrecht, Netherlands.

Tape, C. (2014), Seismic wavefield simulations of earthquakes within a complex crustal model for Alaska, Abstract presented at the 2014 SSA Annual Meeting, Anchorage, Alaska, April 30 - May 2.

Tape, C., Q. Liu, A. Maggi, and J. Tromp (2010), Seismic tomography of the southern California crust based on spectral-element and adjoint methods, Geophys. J. Int., 180, 433–462.

Thio, H. K., R. W. Graves, P. G. Somerville, T. Sato, and T. Ishii (2004). A multiple time window rupture model for the 1999 Chi-Chi earthquake from a combined inversion of teleseismic, surface wave, strong motion, and GPS data, J. Geophys. Res. B Solid Earth Planets, doi:10.1029/2002JB002381.

van Driel, M., L. Krischer, S. C. St ahler, K. Hosseini, and T. Nissen-Meyer (2015), Instaseis: instant global seismograms based on a broadband waveform database, Solid Earth, 6, 701–717, doi:10.5194/se-6-701-2015.

Wang, R., Martin, F.L. and Roth, F., 2003. Computation of deformation induced by earthquakes in a multi-layered elastic crust--FORTRAN programs EDGRN/EDCMP: *Computers & Geosciences*, **29**, p. 195–207.

Wang, R., Lorenzo-Martín, F. and Roth, F., 2006. Erratum to: 'Computation of deformation induced by earthquakes in a multi-layered elastic crust—FORTRAN programs EDGRN/EDCMP': *Computers & Geosciences*, **32**, p. 1817, doi: 10.1016/j.cageo.2006.02.018.

Watada, S., S. Kusumoto, and K. Satake (2014). Traveltime delay and initial phase reversal of distant tsunamis coupled with the self-gravitating elastic Earth, *J. Geophys. Res. B Solid Earth Planets*, n/a–n/a, doi:10.1002/2013JB010841.

West, M. E., P. J. Haeussler, N. A. Ruppert, and J. T. Freymueller (2014), Why the 1964 great Alaska earthquake matters 50 years later, Seismol. Res. Lett., 85(2), 245–251, doi: 10.1785/0220140020.
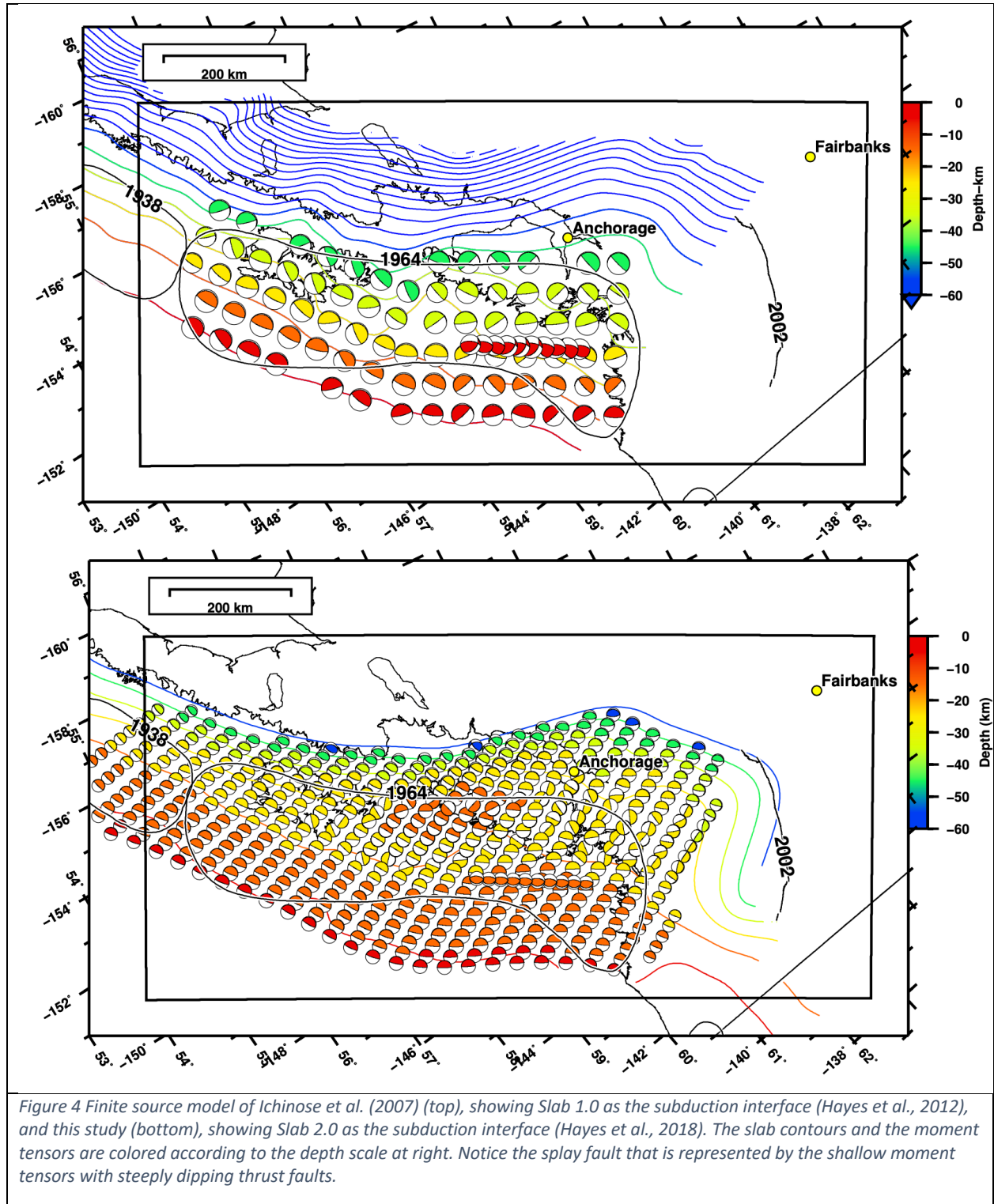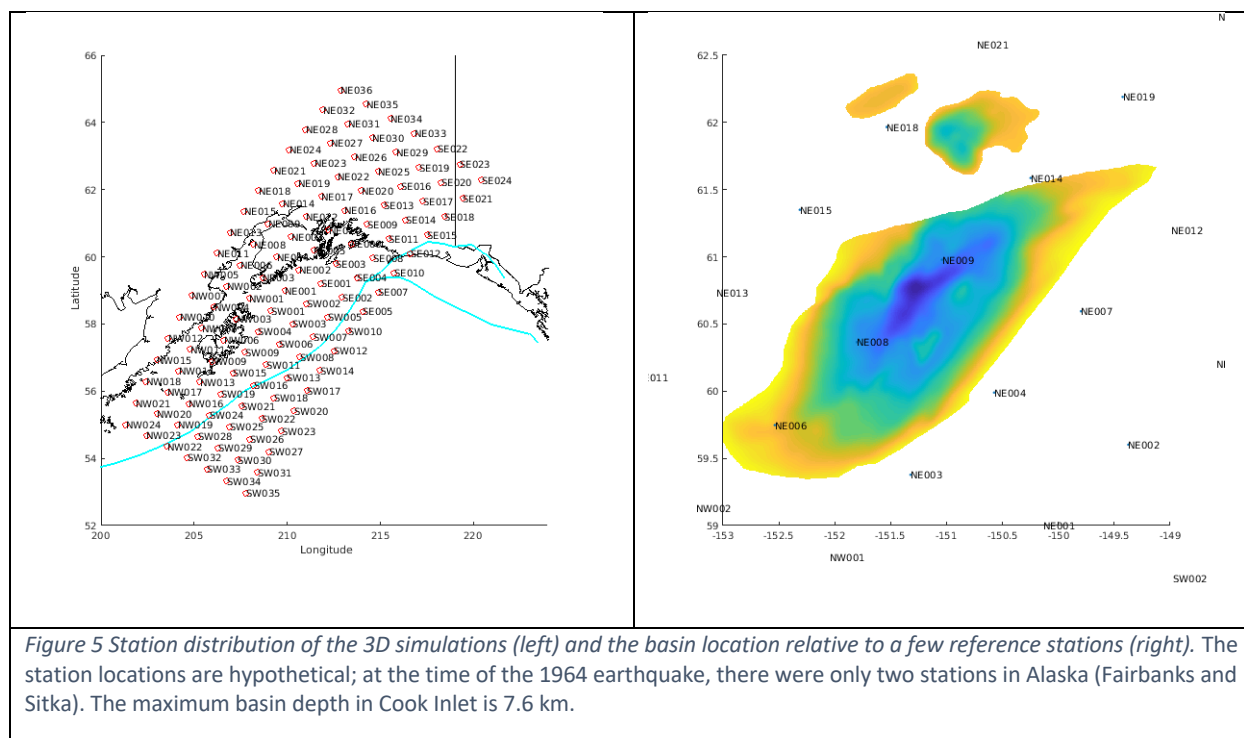
Figures

Figure 1 Map of the 1964 Alaska rupture zone showing the inversion/modeling subfaults (red lines) and the high-resolution patches that constitute the individual subfaults (blue dots). The green line shows the approximate rupture extent from previous studies.

Figure 2 Examples of slip distributions from the inversion of the available data for a range of rupture velocities, smoothing and other parameters. Results on the left are for decreasing smoothing whereas results on the right show increasing rupture velocity from 2.25 to 2.75 km/sec.

Figure 3 Example of waveform fits for the different solutions. Left: seismograms at Hong Kong (top) and La Paz (bottom). Right: tide gauge records at Hilo (top) and Avila Beach (bottom).

Figure 4 Finite source model of Ichinose et al. (2007) (top), showing Slab 1.0 as the subduction interface (Hayes et al., 2012), and this study (bottom), showing Slab 2.0 as the subduction interface (Hayes et al., 2018). The slab contours and the moment tensors are colored according to the depth scale at right. Notice the splay fault that is represented by the shallow moment tensors with steeply dipping thrust faults.
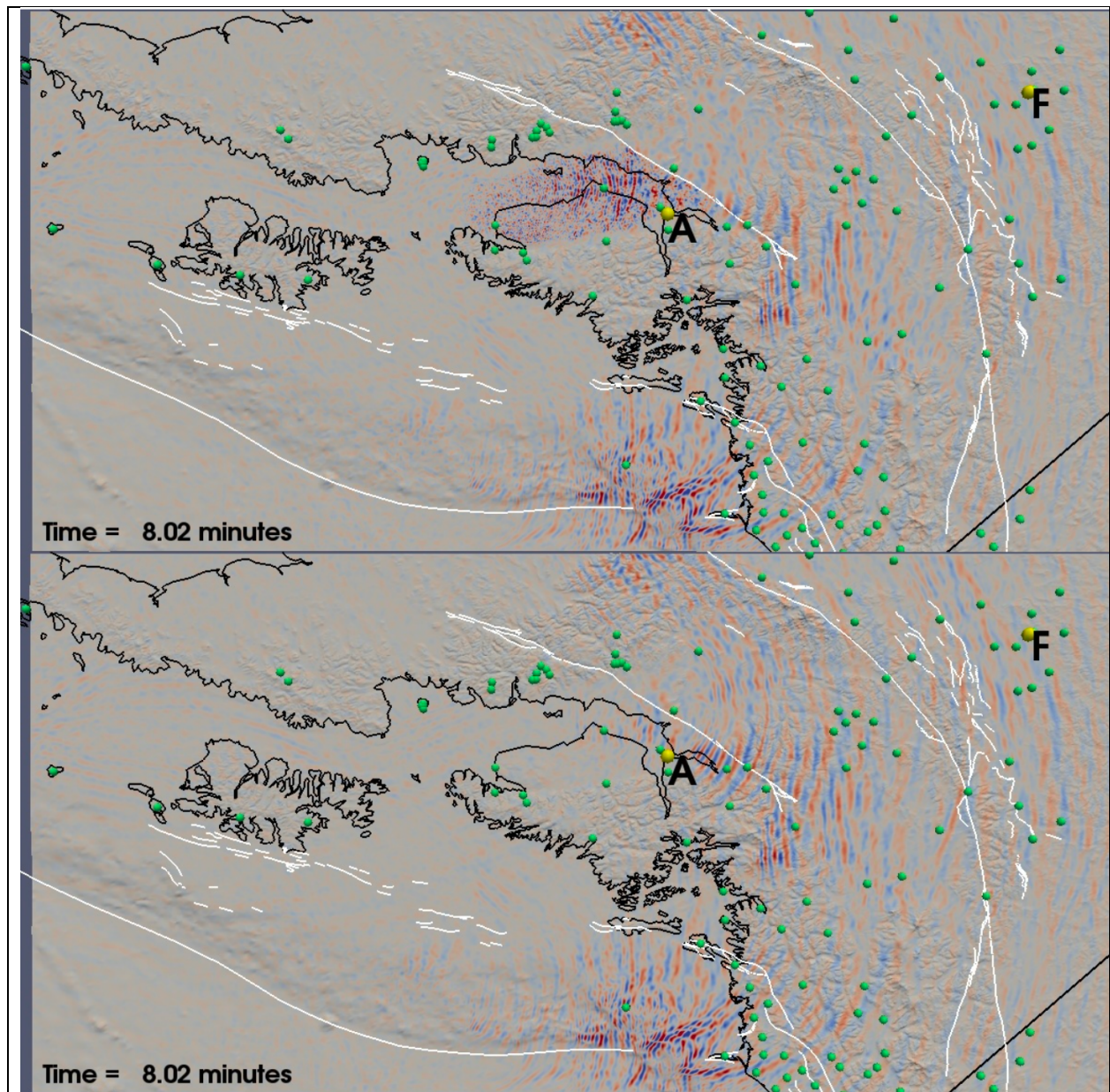
Figure 5 Station distribution of the 3D simulations (left) and the basin location relative to a few reference stations (right). The station locations are hypothetical; at the time of the 1964 earthquake, there were only two stations in Alaska (Fairbanks and Sitka). The maximum basin depth in Cook Inlet is 7.6 km.

Figure 6 The effect of Cook Inlet basin (west of Anchorage) on the seismic wavefield from the 1964 earthquake, demonstrated from previous work. The seismic velocity model in the bottom panel is that of Eberhart-Phillips et al. (2006). In the top panel, a detailed model of the Cook Inlet basin geometry (Shellenbaum et al., 2010) is embedded within the model of Eberhart-Phillips et al. (2006). The wavefield snapshot is at 8 minutes after the origin time. The effect of Cook Inlet basin is more pronounced for local earthquakes than it is for earthquakes on the subduction interface.
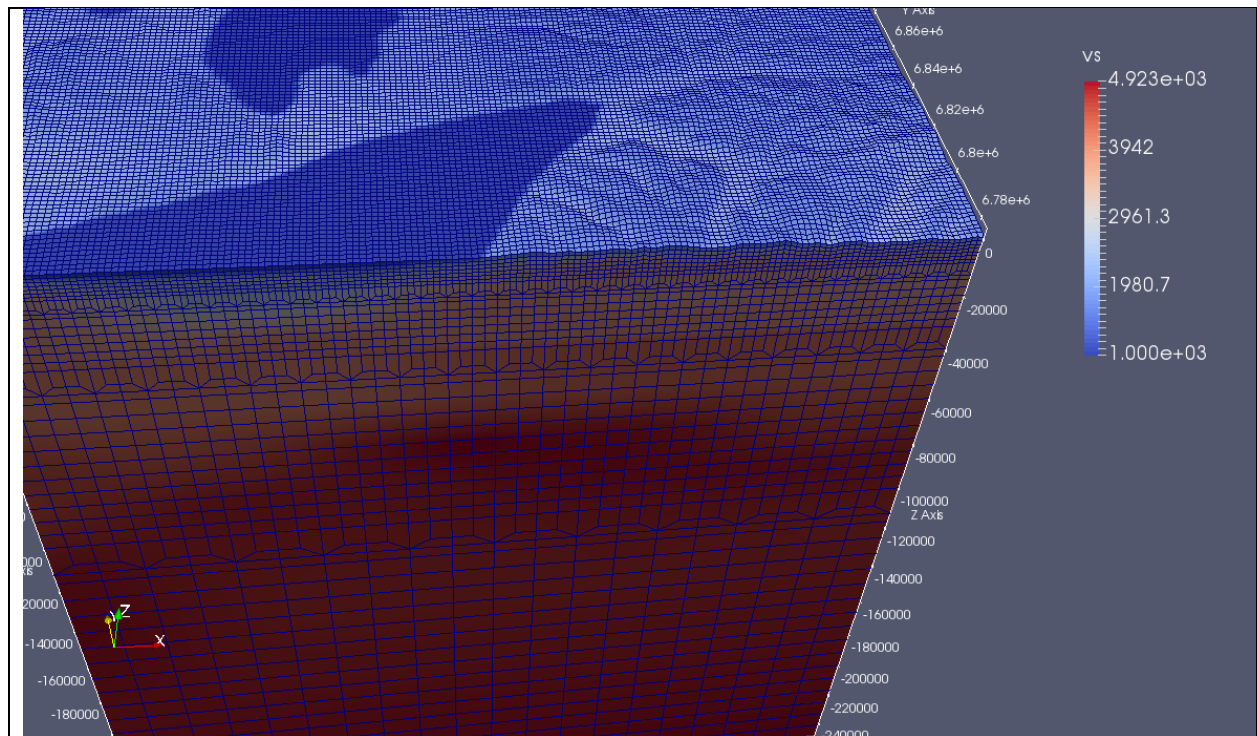
Figure 7 Portion of the 3D finite-element mesh and 3D tomographic model used for seismic wavefield simulations of the 1964 earthquake. The mesh contains three doubling layers, where the element widths double in size (and the element volumes change by a factor of about 8). The tomographic model shown is that of Nayak et al. (2020) with the embedded Cook Inlet basin model of Shellenbaum et al. (2010).
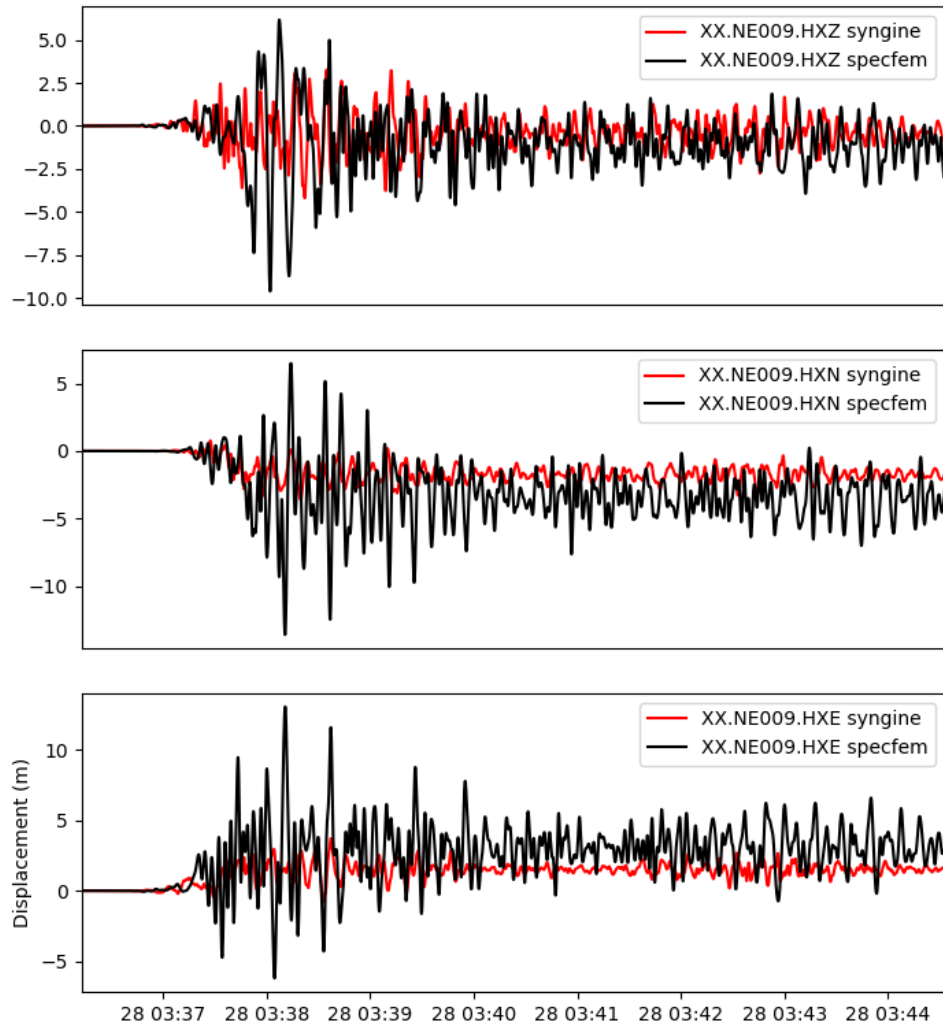
Figure 8 Example of 1D (red) vs 3D (black) waveform comparisons in the basin. The waveforms in the basin exhibit extreme amplitudes and extended duration, especially on the horizontal components. Compare with Figure 9.
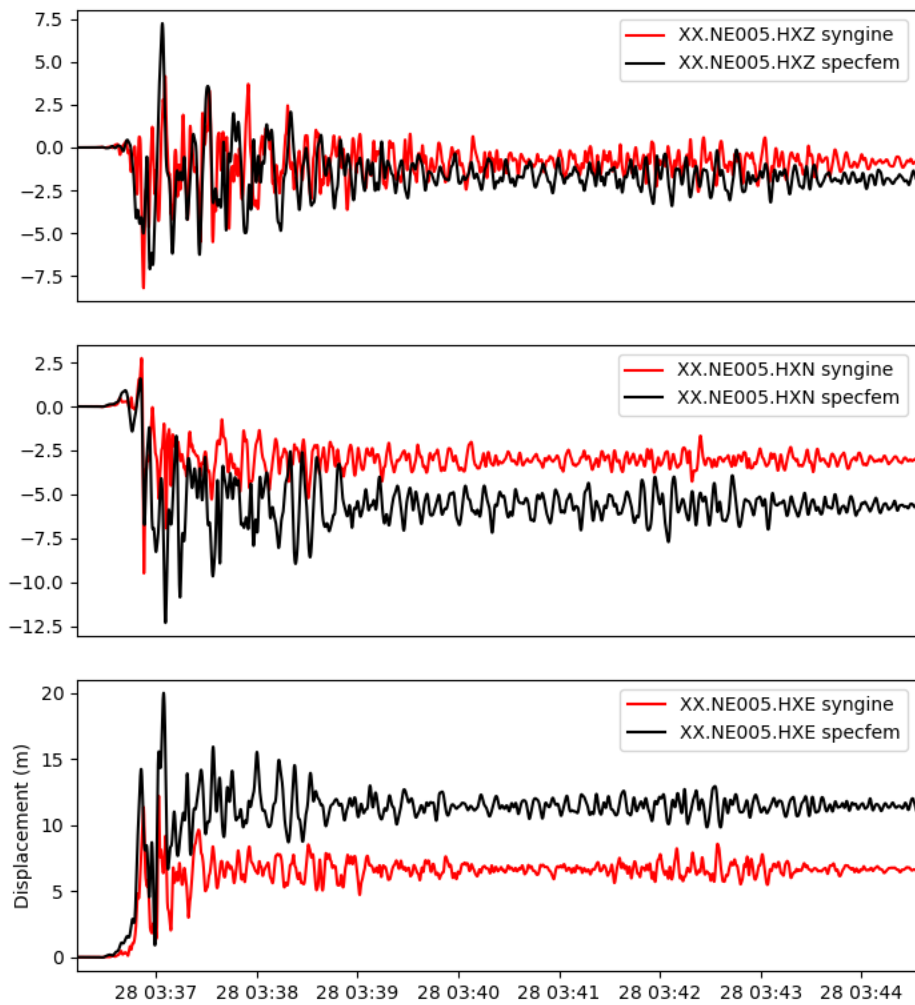
Figure 9 Example of 1D (red) vs 3D (black) waveform comparisons for a station outside Cook Inlet basin. Although the waveforms exhibit similarities, the horizontal static offsets differ by several meters.
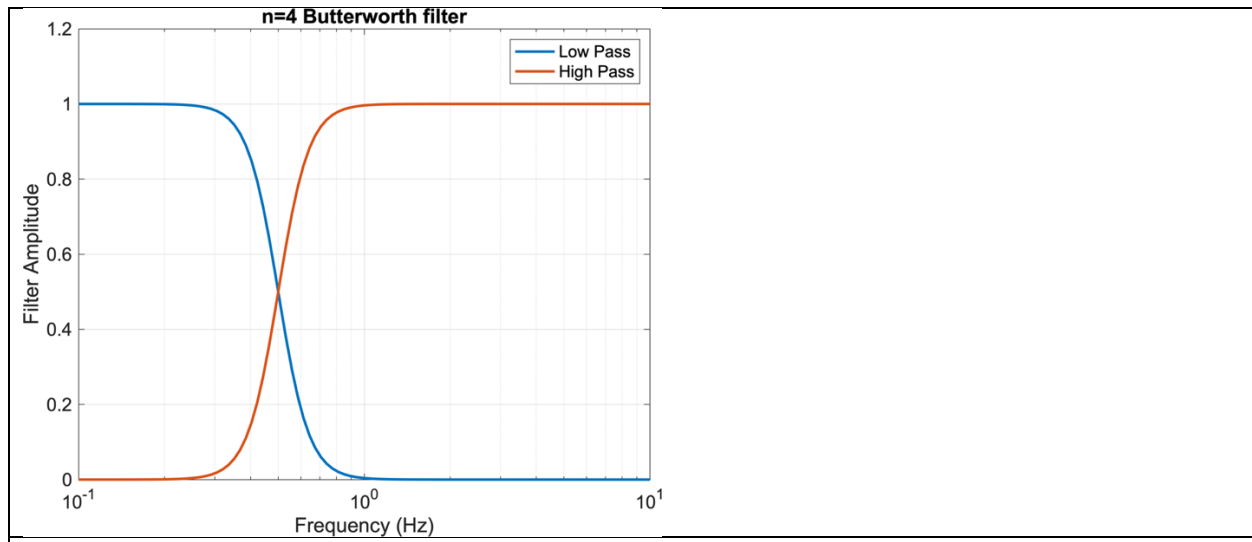
Figure 10 Matched filter used in the combination of the 3D and stochastic waveforms..
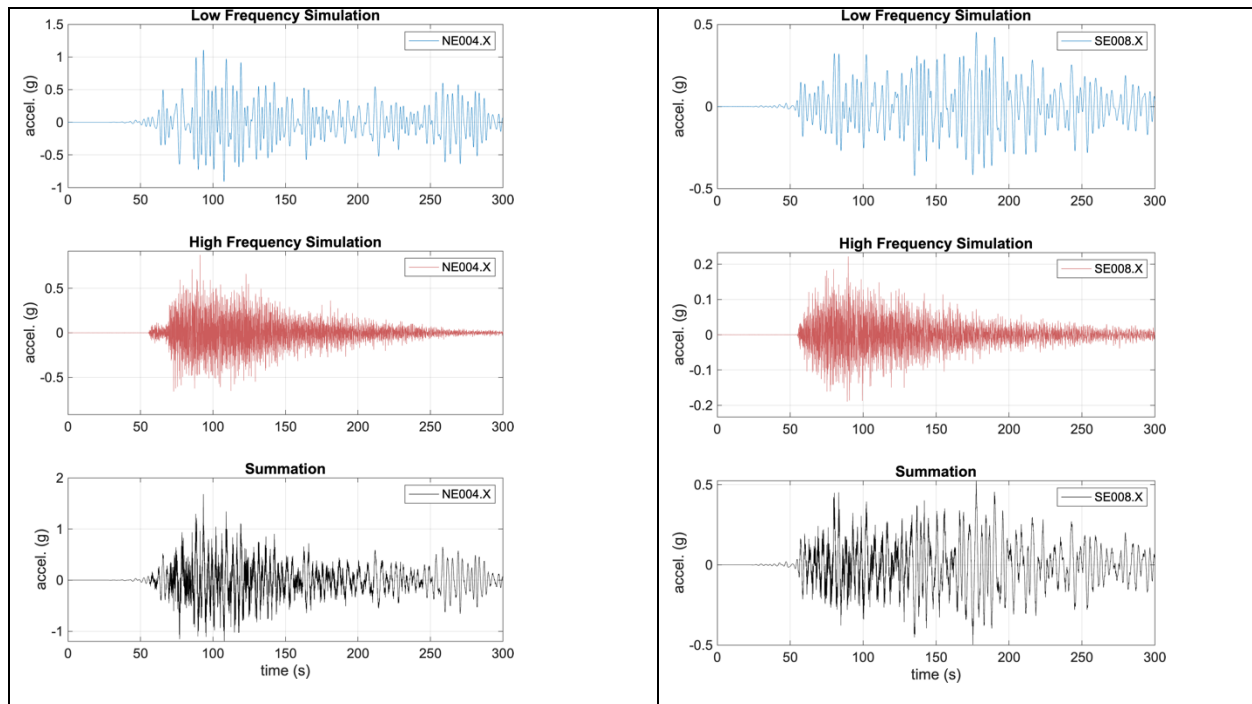

Figure 11 Example of the addition of the stochastic signal based on the Graves and Ptarka method for the first inversion result.